Relation between material structure and photoluminescence properties in yttrium–aluminum borates phosphors

Mathieu Salaun, A Sontakke, V Maurel, J Mouesca, A Barra, V Guimaraes, V Montouillout, B Viana, I Gautier-Luneau, Alain Ibanez

Relation between material structure and photoluminescence properties in Yttrium–aluminum borates phosphors

M. Salaün[1], A. D. Sontakke[2], V. Maurel[3], J.M. Mouesca[3], A. L. Barra[4], V. F. Guimaraes[1], V. Montouillout[5], B. Viana[2], I. Gautier Luneau[1], A. Ibanez[1]

[1] Université Grenoble Alpes, CNRS, Grenoble INP, Institut Néel, F-38000 Grenoble
[2] PSL Research University, Chimie ParisTech - CNRS, Institut de Recherche de Chimie Paris, 75005 Paris, France.
[3] Université Grenoble Alpes, CEA, CNRS, IRIG, SyMMES, 38000 Grenoble (France).
[4] Laboratoire National des Champs Magnétiques Intenses, UPR CNRS 3228, Université Grenoble Alpes 38042 Grenoble (France).
[5] CEMHTI, CNRS UPR3079, Université Orléans, F-45071 Orléans, France.

Abstract:

Glassy yttrium and aluminum borate powders (g-YAB) were synthesized by the polymer precursor method (modified Pechini). We report here a detailed study of the structural, spectroscopic and optical characterizations of the g-YAB powders, involving several complementary techniques: thermal analysis, X-ray powder diffraction and electron microscopy combined with IR, nuclear magnetic resonance and electron paramagnetic resonance spectroscopies. All these results, directly correlated with the photoluminescence (PL) properties of the g-YAB phosphors, allow us to argue that the PL emissions come from large polyaromatic molecules auto-generated from organic precursors and trapped in the glassy network of the g-YAB during thermal treatments. These extended aromatic molecules (7 rings and more corresponding to polycyclic aromatic hydrocarbons) must have been produced during the pyrolysis treatment of the powders, in which a large fraction of the protons were replaced during the calcination process by hydroxyl groups, or other oxygen-containing groups.

1 Introduction

Light-emitting diodes (LEDs), through their high emission efficiency, are increasingly replacing compact fluorescent lamps and fluorescent tubes for indoor lighting, with a 26% reduction in energy consumption, as well as outdoor sodium lamps, with an energy saving of 40-60% [1,2]. Other objectives in the development of this breakthrough technology are the reduction of production costs, the simplicity of white light emitting diodes (wLEDs), their durability and emission colorimetry, but also their applicability for intelligent lighting devices [3,4]. The majority of wLEDs are phosphor-converted LEDs (pc-LEDs), involving phosphors based on metal activators [5]. Moreover, the most dominant pc-LEDs device to produce white light is based on a InGaN chip emitting in the blue, which is partially down-converted to yellow by the $Y_3Al_5O_{12}:Ce^{3+}$ ($YAG:Ce^{3+}$) phosphor [6]. Even if these wLEDs are widely commercialized due to competitive production costs and high photoluminescence (PL) efficiencies, the orange-red spectral deficit of the $YAG:Ce^{3+}$ phosphor produces cold-white emissions associated with an intense narrow PL band in the blue range. This leads to blinding and uncomfortable lighting for eyes with poor color-rendering indexes (CRI = 70-80) [7]. In addition, the intense blue emission component, at about 455 nm, can cause potential damages to the retina and influence human physiology [8,9]. To avoid these serious drawbacks, a large effort is in progress for the development of new phosphors to produce comfortable and safe lightings based on warm white emissions. Indeed, in pc-LEDs, phosphors are a crucial constituent (around 20% of the production cost) involving high purity and expensive rare earths (Ce, Eu,…) or transition metals (Mn) for the doping of oxides, nitrides, oxy-nitrides, fluorides and oxy-fluorides matrices [3,10].

In this context, an emerging route is to use a full-color emitting single-phase, and particularly phosphors involving structural defects acting as emitting centers. These *defect-related* luminescent materials, which can be crystalline or amorphous phases, are a promising

alternative due to their wide and tunable emission bands combined with good stabilities [11]. Indeed, pioneering studies on silica-based materials [12–15] demonstrated that this kind of phosphors can produce broadband emissions in the visible with significant PL internal quantum yields (iQY around 0.2 - 0.45) under near UV excitation (365 nm), while this bluish-white PL was ascribed to carbon-related defects [12]. Several metal oxides have been then studied as zirconates [16], aluminates [17–19] aluminum-silicates [20], tungstates [21,22] and tin or zinc oxides for examples [23,24]. Finally, works on boronitrides or borooxynitrides compounds (BN or BNO phosphors) have shown that carbon doping enhances the PL intensity [25,26].

The PL mechanisms involved in these defect-related materials are not yet fully understood and it is suggested that these PL emissions come from specific defects, or impurities, such as non-bridging oxygen atoms, oxygen vacancies, interstitial carbon atoms, carbons dots and other carbonaceous species [12,20,27,28]. These defects can generate energy levels within the bandgap of the matrix that could be involved in the PL process. Moreover, these previous results have shown that this new family of phosphors is promising for the development of solid-state lighting devices as they can be easily prepared at the micro or nanoscale from solution processes. Nevertheless, these phosphors exhibit usually blue or bluish-white PL emissions corresponding to cold lightings.

Based on these first studies of defect-related PL materials, we have undertaken the development of a new family of amorphous aluminum borate phosphors [29–31]. Our main objectives on these original glassy compositions are to favor wide band emissions in the whole visible range and high concentrations of emitting centers to enhance the PL efficiency. We started from glassy yttrium aluminum borate powders (g-YAB) synthesized by the polymeric precursor route. These g-YAB powders have a composition close to the stoichiometry of c-YAB crystal ($YAl_3(BO_3)_4$), which exhibits a wide bandgap of around 6.2

eV. In addition, aluminum borate systems exhibit extended glass-forming regions and a high diversity of short and intermediate range orders: aluminum can be in AlO_4, AlO_5 and AlO_6 sites [32–34], while boron can form a large variety of chains or rings based on BO_3 and/or BO_4 basic units [32–34]. This could favor adjustments of PL properties towards broad PL bands in the whole visible region to produce warm-white emissions [30]. On the other hand, as previously observed in BN or BNO phosphors, carbon impurities could be inserted in boron sites, thus increasing the concentration of structural defects and enhancing the related PL efficiency [11,35]. Finally, aluminum borates matrices are stable, non-toxic, constituted by abundant elements and can be produced inexpensively on a large scale by several approaches, such as polymeric precursor methods or sol-gel chemistry [35].

These initial hypotheses and statements were confirmed by the first promising results obtained with these phosphors exhibiting warm white emissions through extended PL bands in the whole visible range with high internal quantum yields under NUV excitation at 365 nm and high color rendering indexes [29–31,36]. Moreover, these phosphors exhibit excellent thermal and chemical stabilities. We also specified that the PL efficiency of g-YAB powders are correlated with paramagnetic centers evidenced by Electron Paramagnetic Resonance (EPR) [29]. Nevertheless, the exact nature of emitting centers in such promising PL materials is not yet accurately identified. Recently, we performed a parallel study on g-YAB powders prepared by the sol-gel method, which allowed us to identify molecular fluorescent centers trapped in the amorphous yttrium aluminum borate network [37]. In order to compare these first original results on the accurate determination of PL centers in these phosphors, here we report a detailed investigation on structural, spectroscopic and optical characterizations of g-YAB powders, involving several complementary techniques: thermal analysis, X-ray diffraction and electron microscopy combined with IR, nuclear magnetic resonance (NMR) and electron paramagnetic resonance (EPR) spectroscopy. These results were directly

correlated with the PL properties of g-YAB phosphors in order to specify the origin of their PL emissions.

2 Experimental

2.1 Powder syntheses and thermal treatments

g-YAB powders were synthetized by the polymeric precursor method (modified Pechini) [29]. The resins were prepared by dissolving the precursors in deionized water at 80°C during 30 minutes under stirring, involving two solutions: (1) $Y(NO_3)_3 \cdot 6H_2O$ (2.68g, 7mmol, 99.9%, Strem Chemicals), $Al(NO_3)_3 \cdot 9H_2O$, (7.88g, 21 mmol, 99.8%, Fischer Scientific) and citric acid (32.28g, 168 mmol, 99.5%, Sigma-Aldrich) were dissolved in 50 mL of water, (2) boric acid, (H_3BO_3, 1.73g, 28mmol, 99.8%, Fischer Scientific) and d-sorbitol (20.40g, 112 mmol, 99.5%, Sigma) were dissolved in 50 mL of water. D-sorbitol was preferred to ethylene glycol, generally used in the original Pechini method [38], as it favors the incorporation of boron atoms in the polymeric chains and avoids boron losses (B_2O_3) during thermal treatments. The molar ratio between citric acid:Y:Al:B:d-sorbitol was kept to 24:1:3:4:16. These two initial solutions were then mixed together and placed under reflux at 120^{o}C during 44 hours until the color of the solution turned yellow-orange. Then, the solution was evaporated at 80^{o}C for several hours to reach about 40% of the initial volume, leading to a yellowish and viscous resin due to the polymerization of reagents (polyesterification reactions). The resins dried at 250 °C, during 30 min under air atmosphere, were crushed by ball milling to obtain fine amorphous brown powders called *primary precursor powders*. Such organic-rich powders were gradually oxidized through a two-step treatment [39] to avoid uncontrolled self-combustion, which can generate chemical inhomogeneities. First, the *primary precursor* powders were pyrolyzed, 24 h under nitrogen at 700°C using a heating rate of 30°C h^{-1}, to gradually decompose organic moieties through controlled oxidation reactions. This

intermediate partial oxidation led to amorphous black powders, the *pyrolytic precursor*s, which are subsequently crushed and sieved at 20 μm. Finally, powders were calcined at different temperatures (T_{Ca}) using a heating rate of 30°C h^{-1} with a dwell at T_{Ca} for 10 minutes under a 10 mL min^{-1} O_2 flux leading to luminescent beige powders (final g-YAB powders).

2.2 Characterization methods

To evaluate the glass transitions and crystallization temperatures of the final g-YAB powders, differential thermal analysis (DTA), and thermogravimetry were carried out with a SETARAM TAG 16 equipment, using 30 mg samples within 100 μL alumina crucibles and a heating rate of 5°C min^{-1}. These thermal analyses were directly coupled to a HIDEN analytical apparatus (QGA-HAL201-RC) mass spectrometer to analyze the gaseous by-products of decompositions.

The structural evolutions of powders prepared at different calcination temperatures (T_{ca}) were analyzed by X-ray powder diffraction (XRPD). These XRPD measurements were performed at room temperature in θ - θ geometry using a Bruker Endeavour D8 equipment, operating at 40 kV and 45 mA, using Cu $K\alpha_1$ radiation (1.5406 Å) with a sample holder spinning at 30 rpm. The XRPD scans were collected from 10 to 80^o (2θ), with an increment of 0.032°. Fourier transform infrared (FTIR) spectra were recorded using a spectrometer Bruker Vertex 70V equipped with a liquid N_2 cooled detector (spectral resolution 4 cm^{-1}). The final spectra were obtained by averaging 128 scans, using as sample shaping the dried KBr embedding technique: pellets with 1 wt% of g-YAB powders. The FTIR measurements were carried out under vacuum to avoid any atmospheric pollution. g-YAB powders were also characterized by ^{11}B and ^{27}Al high resolution solid-state MAS-NMR on a Bruker 750WB spectrometer (B_0 = 17.6 T) operating at 240 and 195.3 MHz for the ^{11}B and ^{27}Al nuclei, respectively, with a spinning rate of 30kHz (2.5mm rotors). 1D ^{27}Al spectra have been acquired after a single short pulse (π/10) ensuring a quantitative excitation and quantification of central transition.

^{11}B spectra were acquired with a rotor-synchronized Hahn-echo sequence and a low radio-frequency field strength to ensure a selective excitation of the central transition (ν_{RF} = 10kHz). The ^{11}B and ^{27}Al chemical shifts were referenced relative to $BF_3{\cdot}OEt_2$ and $Al(NO_3)_3$ 1M solutions, respectively. All the spectra were simulated using the DMfit software [40].

Cw-EPR (Continuous-wave electron paramagnetic resonance*)* spectra recorded at X-band were obtained with a Bruker EMX spectrometer operating with an ER-4116 dual mode resonator. They were measured at T = 80 K using an ESR-900 flow cryostat of Oxford Instruments. Typical settings were: 9.655 GHz frequency, 0.02 mW power, and 3 G modulation amplitude with an overall accumulation time of 1 h. Cw Q-band spectra were recorded using a Bruker Elexsys 580 spectrometer operating with a ER5106 resonator. They were measured at room temperature, with the following typical settings: 33.676 GHz frequency, 0.005 mW power, 3 G modulation amplitude overall with an overall accumulation time of 1 h. Cw High-Frequency spectra were recorded using a homemade multifrequency spectrometer, operating in double-pass configuration at 255.36 GHz. They were measured in the temperature range 15-50 K with about 3 G modulation amplitude.

Q-band Pulsed-ENDOR Mims experiments were performed using and Bruker Elexsys 580 spectrometer equipped with a Q-Band EN 5107D2 resonator and an ENI 100 W radiofrequency (RF) amplifier. Typical settings for Mims ENDOR experiments: HF Frequency = 33.55 GHz, B=12109 G, room temperature; Pulses durations: pi(RF) = 20 µs, pi/2(HF) = 16ns (for all pulses of the stimulated echo detection pi/2-t-pi/2-T-pi/2-t-echo), delays t = 252 ns (other values 352, 452 and 552 ns were explored), T = 21 µs. The [1 MHz-70 MHz] RF range was explored with the stochastic mode option provided by Bruker, while the shot repetition time = 0.42 ms.

Concerning DFT methodology, all DFT calculations were performed with the ADF (Amsterdam Density Functional) code developed by E. J. Baerends and co-workers [41] using

triple-zeta basis sets (no frozen core). Geometry optimizations were performed *in vacuo* relying on the Generalized Gradient Approximation (GGA) VBP exchange-correlation (XC) potential (VWN + BP) [42] + corrective terms by Becke [43] for the exchange, and Perdew for the correlation [44] with ADF grid precision 6 throughout. We performed calculations of g-tensors and proton (^{1}H) hyperfine coupling constants with the same XC potential, using the relativistic (scalar) ZORA [45] (two-component Zeroth-Order Regular Approximation) option.

Finally, the photoluminescence spectra under continuous excitation were recorded by using a 385 nm NUV-LED (ThorLabs model M385L2) with optical power set to 1 mW. The luminescence signals were recorded by a CCD detector (Avantes - AVASpec-2048 TEC) guided through an optical fiber. High pass filter of 395 nm was used to cut the excitation signals of the 385 nm LED excitation. For PL-PLE map, a broadband emitting Xe lamp (Energetiq EQ-99X) was used, coupled with a Jobin-Yvon monochromator and the emission was collected using the CCD detector for every 5 nm excitation wavelength steps. The excitation lamp and the CCD detector spectral correction was carried out using a UV-enhanced Si-photo-powermeter (Thorlab PM100D) and a calibrated 10 W halogen lamp (Avantes, AvaLight-Hal-Cal).

3 Results and discussion

3.1 Thermal analysis results

Figure 1 shows the DTA curve (black solid line) between 700°C and 1100°C recorded under oxygen flux of a powder previously pyrolyzed at 700°C during 24h and subsequently calcined at 650°C during 10 minutes (see experimental section). Full-scale analysis is presented in figure SI-1. The endothermic peak at 740°C inducing a shift on the baseline is typical of a glass transition temperature (T_g). Then, three exothermic peaks at 825, 850 and ~~950°C~~

1000°C are due to the crystallization of $Al_4B_2O_9$, $(Y,Al)BO_3$ and $YAl_3(BO_3)_4$ (c-YAB) compounds, *respectively, which were* identified by X-ray powder diffraction (see below). The significant temperature difference between T_g and the first crystallization of around 80°C illustrates the good stability of the YAB glassy matrix.

Mass spectrometry (MS), performed on the gaseous by-products (blue for water, pink for CO_2 and orange for CO, Figure 1) indicates that carbon dioxide is released during the second exothermic peak at 850°C, directly related to a mass loss of about 500 ppm (0.05 wt%), as recorded by thermogravimetry (dotted black line). This CO_2 loss is associated to a very weak release of CO. These results indicate that organic moieties are released and subsequently oxidized. These losses of carbonaceous species are favored by the crystallization of the amorphous aluminum borate matrix. Moreover, the continuous slight drift of the global mass loss baseline (dotted black line), observed between 700 to 1100°C, can be attributed through MS gaseous by-products curves: hydroxyl groups released for temperatures below 850°C as observed in figure SI-1, in agreement with FTIR results (see section 3.2), and by the gradual loss of carbonaceous moieties at higher temperatures (see corresponding drifts of H_2O and CO_2 curves in Figure 1). These weak by-products losses are typical to materials prepared from the polymeric precursor route.

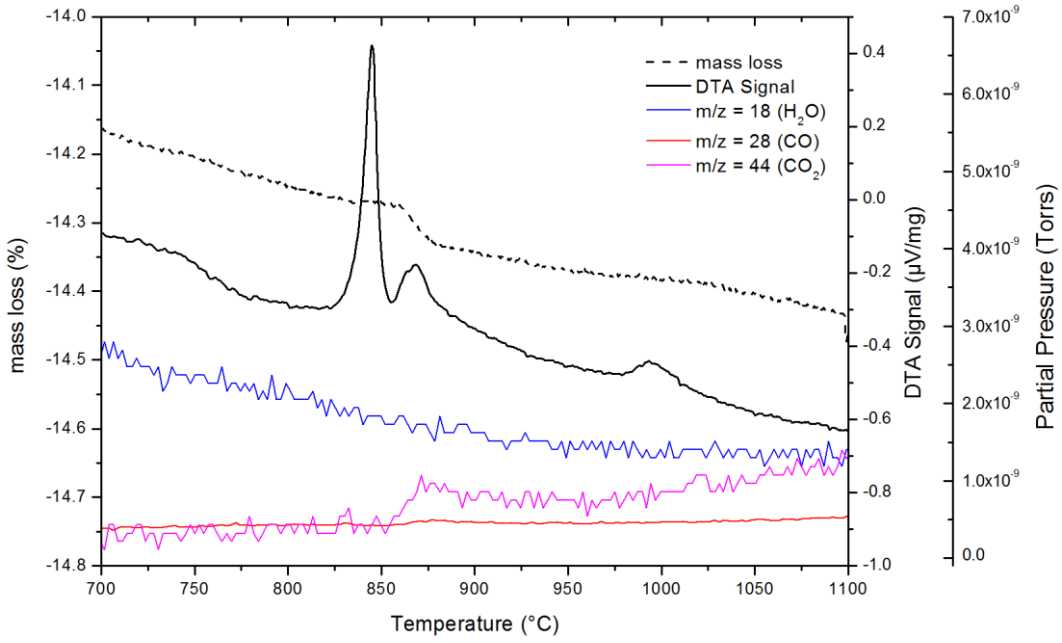

Figure 1: Thermogravimetry (global mass losses) and differential thermal analysis (DTA) of g-YAB powder pyrolyzed at 700 °C/24h/N_2 and calcined at 650 °C/10min/O_2 coupled with mass spectrometry of the main gaseous by-products (water and carbon oxides).

3.2 X-ray powder diffraction (XRPD)

In Figure 2, we can observe that the powders calcined at T_{ca} below 760°C are amorphous as only broad bands of X-ray scattering are observed. Thus, these powdered samples are glasses as they exhibit a clear glass transition temperature, T_g = 740°C, Figure 1. The beginning of powder crystallization was observed by transmission electron microscopy through the occurrence at around 780°C of $Al_4B_2O_9$ nanocrystals embedded in amorphous matrix, Figure SI-2, as confirmed by the XRPD peaks (stars, JCPDS no: 76-8290), (Figure 2). The amount of the $Al_4B_2O_9$ crystalline phase reaches a maximum at around 850°C, decreasing gradually at higher temperatures. At T_{ca} = 825°C, the (Y,Al)BO_3 isostructural form of YBO_3 [6] (circles, JCPDS no: 60-0010) starts to crystallize. Then, YBO_3, (triangles, JCPDS no: 89-3501) and $YAl_3(BO_3)_4$ (squares, JCPDS no: 72-1978) phases appear at around T_{ca} = 850 and 1000°C, respectively. Finally, at 1200°C we obtain the $YAl_3(BO_3)_4$ phase (c-YAB) with remaining traces of YBO_3.

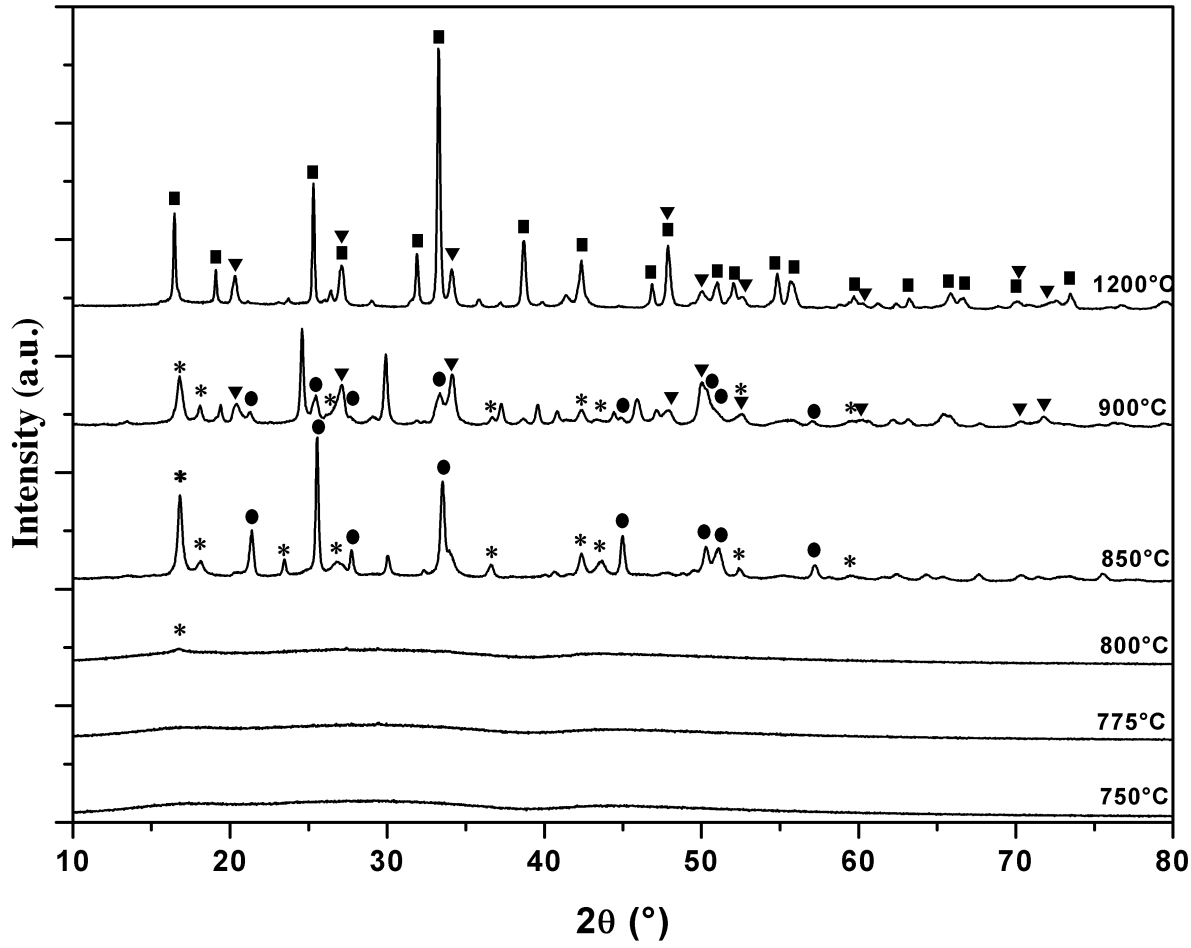

Figure 2: XRPD patterns for powders previously pyrolyzed and then calcined at different temperatures, T_{ca}, specified on each curve.

3.3 FTIR spectroscopy

Figure 3 shows FTIR spectra evolutions versus T_{ca} recorded between 600 and 2200 cm^{-1}. For powders calcined at T_{ca} ranging between 500 and 800°C, the spectra are rather similar and constituted by broad absorption bands typical of glassy samples. The one at 600-850 cm^{-1} can be ascribed to stretching frequencies of aluminates groups AlO_4, AlO_5 and AlO_6 [46–48]. Moreover, the gradual shift to lower wavenumbers observed for this band when T_{ca} increases is in agreement with an increase on the Al coordination number from 4 to 6 [49].

The 600-800 cm^{-1} absorption can also be due to bending vibrations of BO_3 units [50,51]. Thus, all these absorptions cannot be clearly distinguished in the 600-850 cm^{-1} wide band.

The bands appearing in the 950-1150 cm^{-1} region are attributed to B–O stretching vibrations of BO_4 tetrahedral units, which should be associated to the eventual presence of di-, tri-, tetra- and penta-borate groups in the glassy aluminum borate network [52]. The 1200-1500 cm^{-1} absorption bands originate from B–O asymmetric stretching in trigonal BO_3 units existing in metaborate chains and rings, pyroborates and orthoborates structural arrangements. Finally, the 1200-1500 cm^{-1} band can be directly related to the presence of BO_3 units.

At T_{ca} = 850°C, one can observe absorption reductions at around 810-820 cm^{-1} and 960 cm^{-1}, which are probably related to the relative amounts decrease of AlO_4 and BO_4 compounds. This can be explained by significant structural evolutions during the powder crystallization with the gradual transformation of both types of AlO_4 and BO_4 tetrahedral units into AlO_5 or AlO_6 and BO_3 surroundings, respectively. This is in agreement with You *et al*. [47] and Maia *et al*. [53] and the beginning of $Al_4B_2O_9$ crystallization observed by XRPD, which is composed basically with AlO_5 and AlO_6 and the large majority (80%) of BO_3 groups [54]. Then, in order to better specify these Al and B surroundings, solid NMR experiments were performed, see next section.

Finally, the 1600-1700 cm^{-1} band corresponds to the H-O-H bending (delta band) of trapped water molecules in the aluminum borate matrix [55]. This band disappears for $T_{ca} \geq$ 700°C indicating that over this temperature, the g-YAB matrix is anhydrous. This is in good agreement with the evolution of the broad 3200-3600 cm^{-1} band (hydroxyl stretching) with T_{ca}, which disappear completely for T_{ca} above 700°C as seen in figure SI-3.

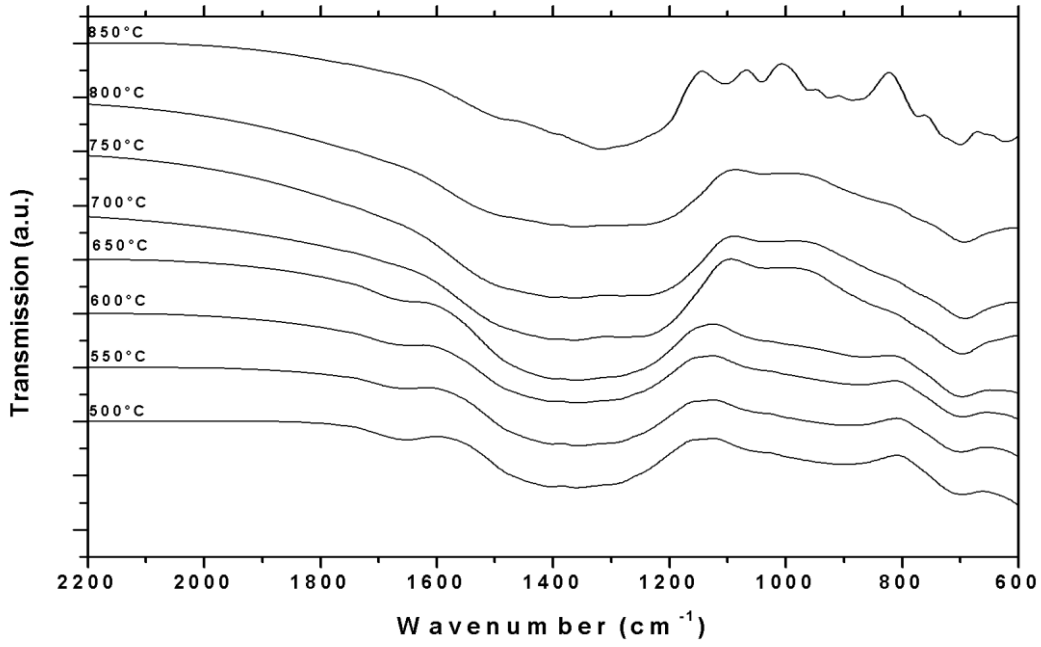

Figure 3: FTIR spectra of g-YAB powders calcined at different T_{ca} between 2200cm^{-1} and 600 cm^{-1}.

3.4 Solid-State Nuclear Magnetic Resonance

Figure 4a shows the ^{27}Al MAS NMR spectra for g-YAB calcined at T_{ca} ranging from 740 to 1180°C. The spectra of powders calcined at 740-760°C show three broad peaks centered at around 4, 32 and 58 ppm, unambiguously assigned to AlO_6, AlO_5 and AlO_4 environments, respectively [32–34]. Their asymmetric line shape are typical of both quadrupolar interactions and chemical shift distribution broadening observed in glassy materials. As the overlapping of the lines renders the quantitative analysis difficult, the analyses were completed by the acquisition of ^{27}Al MQMAS spectra, an example of which is given in figure SI-4a. Based on these two sets of experiments, the spectra were simulated using the DMfit Software [40]. Figure SI-4b shows the deconvolution of the spectra obtained for sample calcined at 740 °C. The NMR parameters as well as the relative proportion of each site are given in Table SI-1. These values do not vary much from 740 to 760°C, indicating that no significant structural change occurs for g-YAB calcined up to 760°C. Above 760°C, as previously observed by X-ray diffraction and TEM experiments, several phases ($Al_4B_2O_9$, $(Y,Al)BO_3$, YBO_3 and

$YAl_3(BO_3)_4$) crystallize, thus inducing huge spectral changes. The spectrum of the sample calcined at 780°C corresponds to the overlapping of the contribution of g-YAB with the spectral signature of crystalline $Al_4B_2O_9$ phase as described by Fisher et al. [54] (figure SI-5). This phase consists of isolated chains of edge-sharing AlO_6 octahedra cross-linked by AlO_4, AlO_5, BO_3, and BO_4 units. In the spectrum of sample calcined at 810°C, no contribution of g-YAB can be detected. The spectrum is dominated by a sharp symmetric line centered at -0.6 ppm, in addition to a small contribution of AlO_4-AlO_5-AlO_6 lines due to the $Al_4B_2O_9$ phase. This new main line corresponds to aluminum six-fold coordinated to oxygen and can be attributed either to $(Y,Al)BO_3$ or to c-YAB ($YAl_3(BO_3)_4$) crystallized compounds. When increasing T_{ca}, the peak becomes narrower while the contribution of $Al_4B_2O_9$ disappear. Finally, at 1180°C only the sharp and symmetric peak of the octahedral sites of c-YAB is observed at -0.3 ppm in agreement with the XRD results, Figure 2.

In the same way, Figure 4b shows the ^{11}B MAS NMR spectra of samples calcined at T_{ca} ranging from 740 to 1180 °C. The high magnetic field used for the acquisition of the ^{11}B MAS NMR spectra results in a complete resolution of BO_4 and BO_3 resonances, in the range of -5 – 5 and 10 – 25 ppm, respectively. For samples calcined at 740 and 760°C, the spectra exhibit two broad Gaussian like peaks with isotropic shifts centered at 1 and 15 ppm. These lines are typical of borate glassy network and correspond respectively to BO_4 (10%) and BO_3 units (90%). As for ^{27}Al MAS-NMR spectra, these broad bands are consistent with the glassy structure of g-YAB powders and no significant changes can be noted in this T_{ca} range. In the case of sample calcined at 780 °C, new BO_3 and BO_4 peaks are observed overlapping with g-YAB contributions. The BO_3 massif becomes complex and difficult to simulate unambiguously, while the BO_4 region is composed of a broad resonance centered at 1.0 ppm due to g-YAB and a narrower signal centered at -1.1 ppm. These results are perfectly

consistent with the presence of $Al_4B_2O_9$ phase [54] as observed by ^{27}Al NMR, TEM and XRPD experiments.

In the spectrum of the calcined sample at 810°C, no further contribution of g-YAB can be detected. The contribution of $Al_4B_2O_9$ phase is observed in addition with new BO_3 signals. These latter are coherent with BO_3 environments described by Deters et al. [32] for c-YAB. Finally, as can be seen on Figure SI-6, the ^{11}B MAS-NMR spectra of sample calcined at T_{ca} = 1180°C can be deconvoluted with two quadrupolar lineshapes (δiso = 18.8 ppm, C_Q = 2.88 MHz, η_Q = 0.07 / δiso = 20.0 ppm, C_Q = 2.99 MHz, η_Q = 0.08) corresponding to the two BO_3 environments of the c-YAB phase [32].

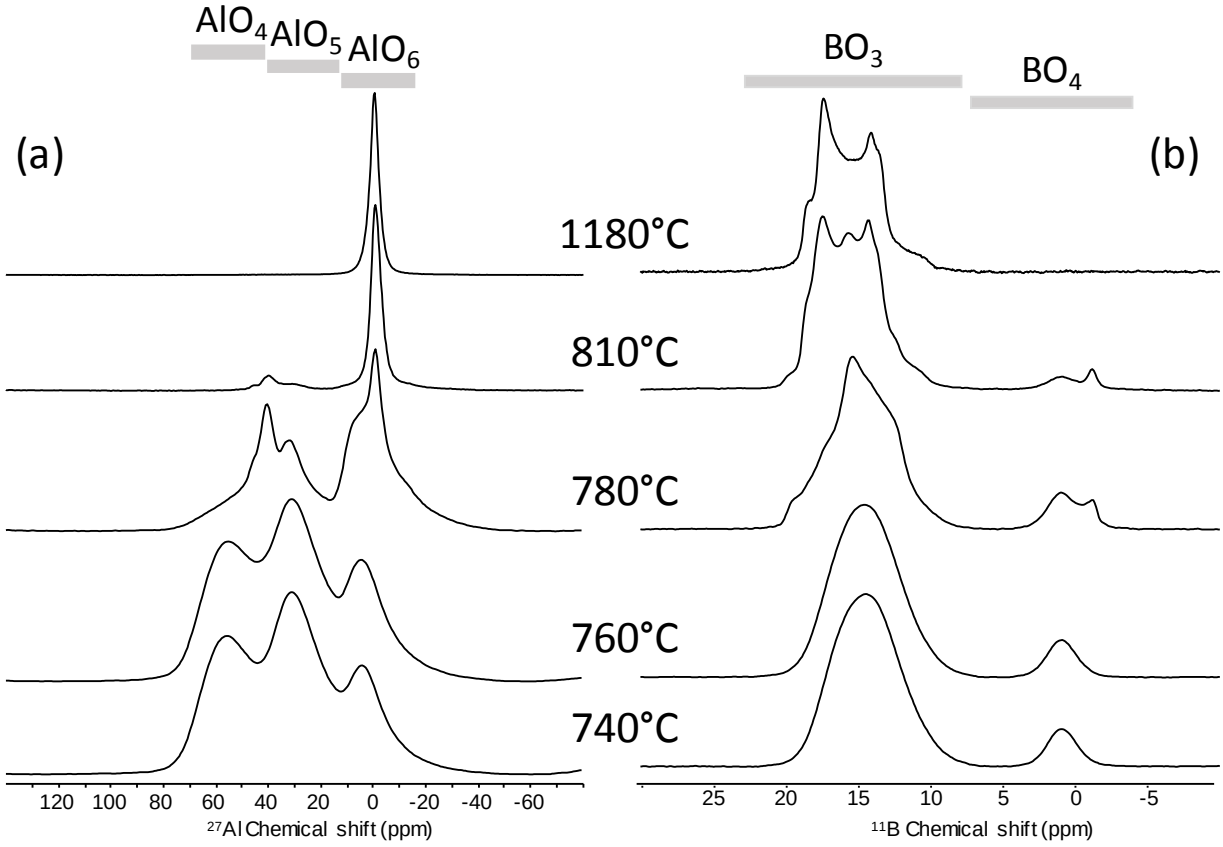

Figure 4: (a) ^{27}Al MAS-NMR and (b) ^{11}B MAS-NMR spectra for g-YAB calcined at T_{ca} ranging from 740 to 1180°C.

3.5 Continuous-wave EPR and pulsed ENDOR spectroscopies

g-YAB samples prepared by using various calcination temperatures ranging from T_{ca} = 500°C, up to 700°C, were first studied by continuous wave EPR through X band (9.65 GHz) at 80 K, Figure 5a. For all these samples a single and narrow (ΔH = 5G peak-to peak) unresolved feature was observed at magnetic field values close to g = 2. The intensity of this feature decreases strongly from T_{ca} = 500 to 700°C, while the shape of this feature is not symmetrical: for all T_{ca}, the absolute maximum is higher in absolute value than its absolute minimum counterpart, which might be due to a more complex structure hidden at X band due the linewidth of the EPR signals. This more complex structure appeared clearly in cw-EPR spectra recorded at Q band (35 GHz). Such spectra had to be recorded at room temperature to avoid the saturation of EPR transitions. The spectra of samples prepared at T_{ca} = 650 and 700°C are shown in Figure 5b. For T_{ca} = 650°C, the EPR spectrum exhibits a main signal centered at g = 2.0055, calibrated by comparison with the DPPH standard (2,2-diphenyl-1-picrylhydrazyl). A shoulder is observed at g = 2.0035. For samples with lower calcination temperatures, spectra with the same shape but higher intensity are observed (data not shown). For T_{ca} = 700°C, the shoulder at g = 2.0035 is much less clearly observed and a quasi-symmetrical spectrum centered at g = 2.0055 remains, with a much lower intensity small feature at g = 2.0013. This evolution of the Q band EPR spectra with T_{ca} pleads for the presence of at least two distinct paramagnetic species having some g tensor components close to g = 2.0055 and 2.0035, rather than for a unique paramagnetic species with an anisotropic g tensor.

This conclusion is also supported by the EPR investigations performed at high frequency (255 GHz). The spectrum recorded for a sample calcinated at 550°C is shown in Figure 5c. At such a high frequency, it was impossible to avoid the saturation of the EPR transition in such

sample. The main signal is strongly distorted, but centered at g = 2.0050 (calibrated with a standard sample of Mn^{2+} diluted in MgO), very close to the main signal observed at g = 2.0055 in Q band. A shoulder is observed at ~0.0015 lower g value, which can correspond to the signal observed at g = 2.0035 at Q Band.

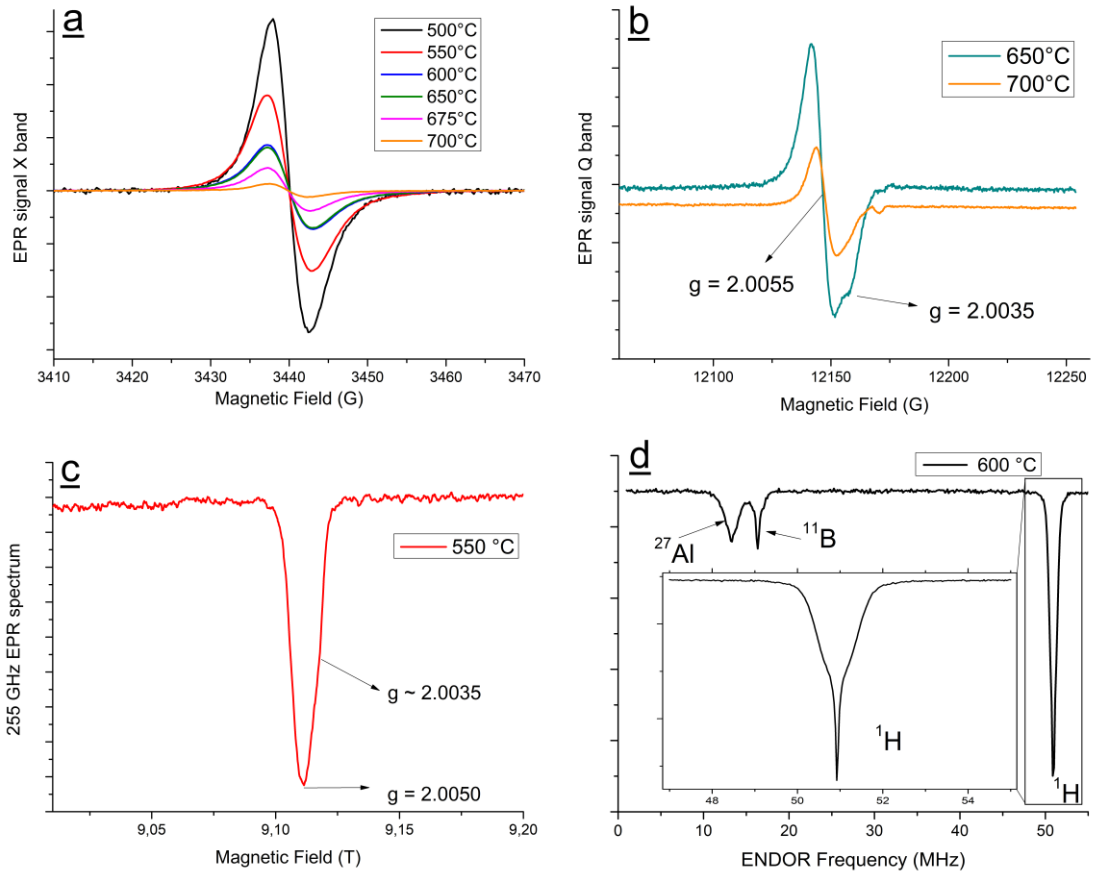

Figure 5: (a) Cw X-band 9.6 GHz EPR spectra recorded at low temperature (80 K) for g-YAB samples calcinated at temperatures ranging from 500 to 700°C. (b) cw Q-band 33.6 GHz EPR spectra recorded at room temperature for g-YAB samples calcinated at 650 and 700°C. (c) cw 255 GHz EPR spectrum recorded at low temperature (T = 15 K) for g-YAB sample calcinated at 550°C. (d) pulsed Q-band Mims ENDOR spectrum recorded at room temperature for g-YAB sample calcinated at 600°C.

No splitting due to hyperfine or quadrupolar interactions with nuclear spins was observed in the X-band, Q-band and 255 GHz EPR spectra. In order to detect putative small hyperfine or quadrupolar interactions, pulsed Q-band Mims ENDOR experiments were performed at the

magnetic field corresponding to the g = 2.0055 EPR signal. A typical spectrum obtained for sample calcinated at 600°C is shown in Figure 5d. Three features are observed, centered at 51 MHz (^{1}H), 13.3 MHz (^{27}Al) and 16.1 MHz (^{11}B). For the three nuclei, a very narrow and more intense component at the Larmor frequency of the corresponding nucleus is attributed to distant nuclei with almost no coupling with the electron spins under study. Apart from these signals due to distant nuclei, only signals corresponding to hyperfine or quadrupolar interactions smaller than 2 MHz for ^{27}Al and 1 MHz for ^{11}B and ^{1}H are observed.

The observed EPR and ENDOR features are completely incompatible with paramagnetic centers centered on boron or aluminum, which would exhibit strong interaction with these nuclei. At first sight, such narrow EPR spectra and very small hyperfine interactions might be compatible with free electrons located in oxygen vacancies. However, the observed g values are significantly higher than the typical values of such electrons in vacancies (typically g = 2.0028), which rules out this hypothesis, at least for the signal observed at g = 2.0055. This suggests that the paramagnetic centers observed here are carbon centered and that at least a fraction of the observed species are containing also some heteroatoms as oxygen, which will contribute to the g-tensors' anisotropy via their spin-orbit constants. On the other hand, the absence of any hyperfine interaction with protons higher than 1 MHz rules out the attribution of the observed spectra to organic free radicals derived from small aromatic molecules (up to 2 or 3 fused rings) similar to those we reported previously in the case of g-YAB phosphors synthetized by the sol-gel method [37]. Thus, the hypotheses that would best correspond to the EPR and ENDOR spectra reported here would be (i) free radicals derived from extended polyaromatic molecules with hydroxyl or other oxygenated groups or (ii) paramagnetic centers in carbon nanoparticles.

In order to explore further the first hypothesis, we succinctly present here DFT computations of g tensors and proton hyperfine coupling constants for our most promising

candidates so far, that is cation radicals derived from a series of fully hydroxylated aromatic molecules of increasing sizes (1-ring/benzene, 7-rings/coronene and 19-rings/circumcoronene aromatic molecules: see Figures 6-7 and Table 1, as well as SI for DFT Methodology details).

We considered the three following models of increasing sizes represented in Figure 6:

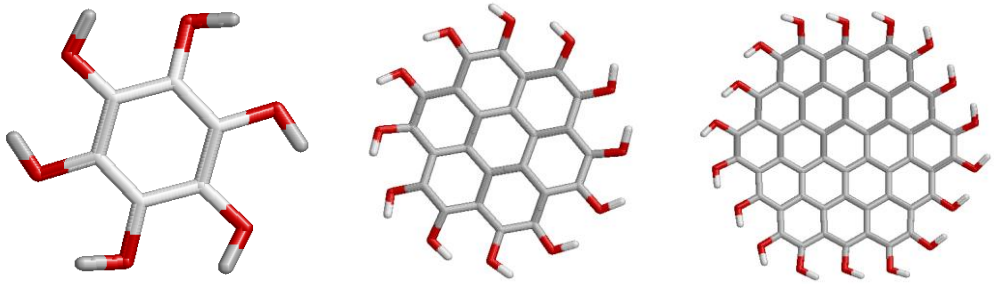

Figure 6: Fully hydroxylated benzene (left: one-ring), coronene (middle: 7-rings) and circumcoronene (right: 19-rings) molecules.

		g_min	g_int	g_max
exp	-	2.0013	2.0035	2.0055
Radical cations	1-ring	**2.0019**	**2.0042**	**2.0059**
	7-rings	**2.0006**	**2.0037**	**2.0052**
	19-rings	**2.0006**	**2.0034**	**2.0051**

Table 1: g-values computed for fully hydroxylated 1-ring, 7-rings and 19-rings cationic models.

Quite interestingly, the DFT computed g tensors reported in Table 1 show that the highest component of the tensors computed for these fully hydroxylated cation radicals consistently reach a value close to the highest experimental g value (2.0055). Moreover, their intermediate g values are close to the second experimental value (2.0035). Finally, minimal g-values for all three models are consistently close to the g value observed for the small experimental feature (2.0013).

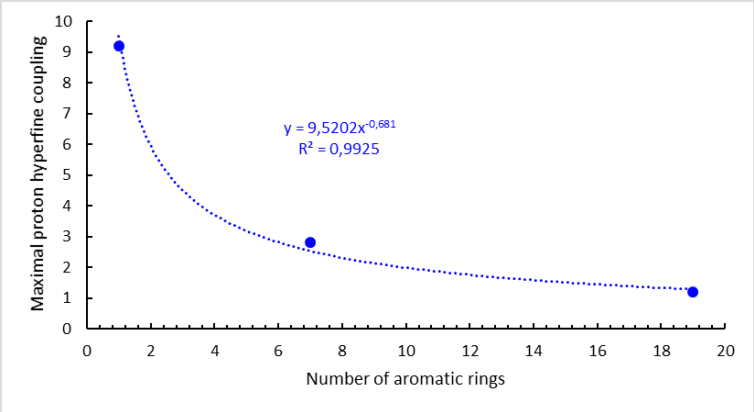

Figure 7: Maximal proton hyperfine coupling constants computed as a function of the size of the aromatic rings (number of rings: 1, 7 and 19, respectively). The best fit corresponds to a power law.

As for the DFT computed proton hyperfine coupling constants, they show that the highest predicted value is significantly lower for the 7-rings model compared with that of the 1-ring model (see Figure 7), the more so for the 19-rings model. With the exception of values computed for the 1-ring model, those values computed for the two larger models are already compatible with the very small couplings (<2 MHz) observed by ENDOR (Figure 5d).

Such tentative comparisons of DFT computations for these three aromatic free radicals of increasing sizes (1-ring, 7-rings, 19-rings: Figure 6) with experimental EPR and ENDOR spectra do not enable us to unambiguously identify the exact structures of the observed paramagnetic centers. Moreover, keep reminded that, experimentally, the two largest observed g components seem to belong to two different species. Still, these DFT calculations, in good agreement with the experimental g values and with a good trend for hyperfine coupling constants for protons, already support an assignment of these spectra to free radicals derived from rather large polyaromatic molecules (~7-rings and higher). These extended polyaromatic molecules, corresponding to polycyclic aromatic hydrocarbons (PAHs) must have been produced during the pyrolysis treatment of powders, in which a large fraction of the protons have been replaced during the calcination process by hydroxyl groups, or other oxygen-containing groups.

Photoluminescence properties

The g-YAB powders exhibit intense and broad PL bands in the visible through near UV excitations. Figure 8 presents the normalized PL spectra of g-YAB powders calcined at different temperatures. For calcination temperature around T_{ca} = 550-600°C, the PL emission is extended in the whole visible range and becomes then narrower as T_{ca} increases from 550°C to 700°C. Moreover, for T_{ca} ranging between 700°C and 800°C, we observed a slight broadening of the PL band, Figure SI-7. These results reveal that the PL properties strongly depend on the calcination temperature of powders. To get a better overview of the emission-excitation properties, the PL-PLE contour maps were recorded and are shown in Figure 9. It is clear from Figure 9a that the powder calcined at 550°C exhibits the broadest PL profile. Moreover, the excitation maximum occurs at around 350-400 nm leading to intense emission in the 400-700 nm range covering most of the visible spectral range. The PL then becomes narrower for T_{ca} = 650°C and 700°C (Figure 9b, c and d) revealing mostly blue emission in agreement with Figure 8. At T_{ca} = 700°C (Figure 9c), the PLE exhibits distinct excitation bands peaking at about 220 nm, 275 nm and 340 nm, respectively corresponding to the 400 nm peak emission. Though the 775°C calcined powder exhibits a slight broadening in PL profile over the 700°C calcined powder, the distinct PLE contours at 220 nm, 275 nm and 340 nm are still clearly seen corresponding to the 400 nm emission. This suggests that the violet-blue emission originates from these PLE bands and that the corresponding emitting centers are the dominant ones in these powders. On the other hand, the PLE bands of the powder calcined at 550°C are not so distinct, but covers the broadband region. The broadening in PL and non-distinct PLE contour represent the presence of multiple emitting centers in 550°C calcined powder with competing weight fractions, so that the individual excitation and emission concomitantly admixes resulting in broad band profile. This is well consistent with the presence of various types of polyaromatic molecules (PAHs) synthesized and embedded

into the YAB glassy network during their formation through the two-step thermal treatments: namely pyrolysis followed by the powder calcination.

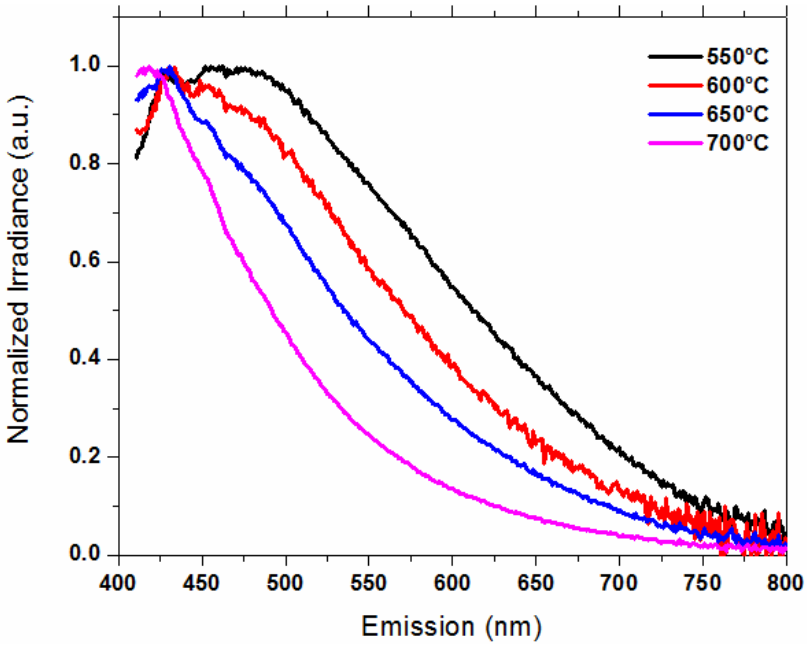

Figure 8: PL spectra as a function of calcination temperature of different YAB powders. High pass filter of 395nm was used to cut the excitation signals of 385 nm LED

It is worth to note here that the PL broadening tendency in present g-YAB powders is not the same as our previously reported g-YAB powders [29,56]. In previous studies, we observed that the PL exhibited broadening until 750°C calcination temperature and then, the PL slightly narrowed down accompanied by a decrease in PL intensity as the powders start to crystallize above 760°C. These differences in the PL properties of this paper powders are related to their smaller average particle size of about 10-20 µm instead to 40-50 µm for previous syntheses. We believe that the oxidation of the carbonaceous species responsible for the blue shift in luminescence occurs at lower temperatures with smaller particle sizes because the solid-gas reactions are strongly dependent on the exchange surface. Indeed, as the particle size decreases, the reactivity of the powders increases and therefore oxidation can occur at lower temperatures than for higher particle sizes. Indeed, to achieve a better control of the synthesis method involving delicate gas-solid reactions, in this study we crushed and sieved the

pyrolytic precursor powder below 20 µm before a short calcination step in pure O_2 atmosphere. In this way, we have tuned the PL properties at a lower temperature (broadest PL at 550°C instead of 750°C in previous synthesis method) and smaller calcination duration (10 minutes instead of 24 hours in previous syntheses).

In conclusion, these first results show that the observed PL spectral evolutions are directly related to the conditions of the two-step heat treatments of powders, and more particularly to the calcination temperature, T_{ca}. Indeed, this parameter is essential because it allows, via solid-gas reactions, to finalize the formation of the host matrix (densification of the aluminum borate network) and simultaneously to form various type of photoluminescent polyaromatic molecules (PAHs molecular emitting centers), as evidenced just above by coupled EPR and ENDOR characterizations and DFT calculations. Thus, depending on $T_{ca,}$ different hydroxylated polyaromatic molecules are generated with different PL spectral emissions, and are trapped (stabilized) in the glassy g-YAB network during its formation.

Finally, the PL internal quantum yields (iQY) of the powders as a function of calcination temperature are given in Figure SI-8. It can be observed that iQY increases with the calcination temperature until a maximum of around 0.6 for T_{ca} = 700°C that is very promising for the development of phosphors for solid-state lighting with this new family of full-color emitting single phosphors.

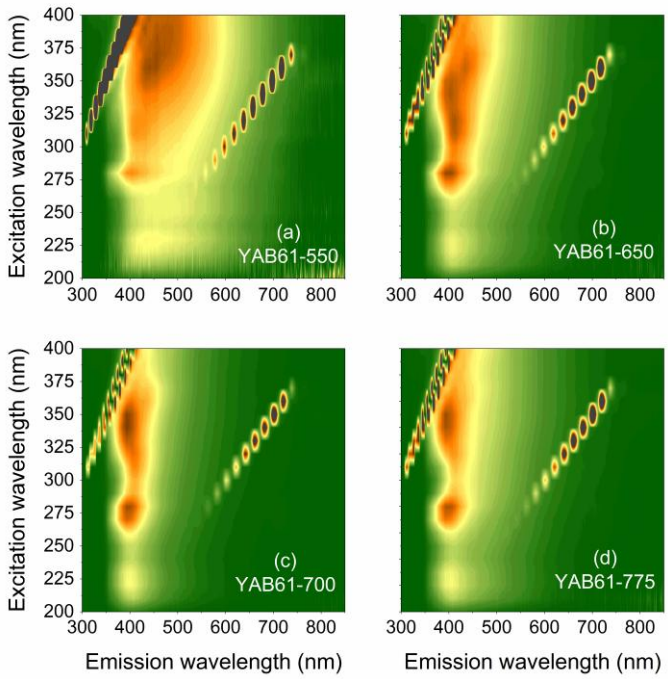

Figure 9: PL-PLE contour plots of g-YAB powders calcined at (a) 550°C, (b) 650°C, (c) 700°C and (d) 775°C. The straight diagonal line features are due to the excitation beam and its overtone as no optical filter was used in this measurement.

Conclusion

As observed by XRPD and NMR, the structural properties of g-YAB powders remain stable until 750°C due to the super-frozen state of these glassy matrices. Above the glass transition temperature, T_g = 740°C, these aluminum borate glasses exhibit visco-elastic properties that allows cationic diffusion followed by the crystallization of the stated phases. Thus, the calcination temperature below T_g does not affect the inorganic glassy structure, but the PL properties of g-YAB powders can be easily tuned. Similar evolution was observed with the EPR signals, which shows close dependence between paramagnetic centers and the calcination temperature, even below T_g. Based on a previous study combining complementary characterization techniques and DFT calculations performed on g-YAB powders prepared by the sol-gel method [37], and this study involving thermal analyses, XRPD, NMR, EPR, PL and DFT calculations performed on g-YAB powders synthesized by the polymeric precursor method, we can argue that PL emissions come from rather large polyaromatic molecules (7-

rings and higher). These polyaromatic molecules (polycyclic aromatic hydrocarbons) are self-generated from organic precursors trapped on the glass matrix during its formation through pyrolysis and calcination treatments. In addition, such specific dependence of PL properties on calcination temperature and duration in oxidizing atmosphere, as well as the role of particle size, hint that the PL is strongly related to solid-gas reactions involving carbonaceous species during thermal treatments under controlled atmospheres. This leads to the formation of hydroxylated polyaromatic molecules, responsible for the PL properties [37], which are strongly confined in the glassy network. Based on this structural knowledge of aluminum borate matrices and the nature of emitting centers as extended polyaromatic molecules, works are in progress to optimize the PL properties, and more particularly the color quality and efficiency of the emissions, which are already promising for phosphor applications.

Conflict of interest statements

On behalf of all authors, the corresponding author states that there is no conflict of interest

References

[1] S.T. Tan, X.W. Sun, H. V. Demir, S.P. Denbaars, IEEE Photonics J. 4, 613 (2012) http://dx.doi.org/10.1109/JPHOT.2012.2191276

[2] E.F. Schubert, J.K. Kim, Science 308, 1274 (2005) http://dx.doi.org/10.1126/science.1108712

[3] S. Ye, F. Xiao, Y.X. Pan, Y.Y. Ma, Q.Y. Zhang, Mater. Sci. Eng. R Reports 71, 1 (2010) http://dx.doi.org/10.1016/j.mser.2010.07.001

[4] D.P. Dutta, A.K. Tyagi, Solid State Phenom. 155, 113 (2009) http://dx.doi.org/10.4028/www.scientific.net/SSP.155.113

[5] P. Pust, V. Weiler, C. Hecht, A. Tücks, A.S. Wochnik, A.K. Henß, D. Wiechert, C. Scheu,

P.J. Schmidt, W. Schnick, Nat. Mater. 13, 891 (2014) http://dx.doi.org/10.1038/nmat4012

[6] A.D. Sontakke, J. Ueda, J. Xu, K. Asami, M. Katayama, Y. Inada, S. Tanabe, J. Phys. Chem. C 120, 17683 (2016) http://dx.doi.org/10.1021/acs.jpcc.6b04159

[7] A.A. Setlur, E. V. Radkov, C.S. Henderson, J.-H. Her, A.M. Srivastava, N. Karkada, M.S. Kishore, N.P. Kumar, D. Aesram, A. Deshpande, B. Kolodin, L.S. Grigorov, U. Happek, Chem. Mater. 22, 4076 (2010) http://dx.doi.org/10.1021/cm100960g

[8] R.G. Stevens, D.E. Blask, G.C. Brainard, J. Hansen, S.W. Lockley, I. Provencio, M.S. Rea, L. Reinlib, Environ. Health Perspect. 115, 1357 (2007) http://dx.doi.org/10.1289/ehp.10200

[9] S.L. Chellappa, R. Steiner, P. Blattner, P. Oelhafen, T. Götz, C. Cajochen, PLoS One 6, e16429 (2011) http://dx.doi.org/10.1371/journal.pone.0016429

[10] US Dept. of Energy, https://www.energy.gov/eere/ssl/downloads/solid-state-lighting-2016-rd-plan

[11] C. Zhang, J. Lin, Chem. Soc. Rev. 41, 7938 (2012) http://dx.doi.org/10.1039/c2cs35215j

[12] W.H. Green, K.P. Le, J. Grey, T.T. Au, M.J. Sailor, Science (80-.). 276, 1826 (1997) http://dx.doi.org/10.1126/science.276.5320.1826

[13] V. Bekiari, P. Lianos, Chem. Mater. 10, 3777 (1998) http://dx.doi.org/10.1021/cm980739w

[14] Y. Ishii, A. Matsumura, Y. Ishikawa, S. Kawasaki, Jpn. J. Appl. Phys. 50, 01AF06 (2011) http://dx.doi.org/10.1143/JJAP.50.01AF06

[15] A. Matsumura, Y. Ishii, K. Sato, Y. Ishikawa, S. Kawasaki, IOP Conf. Ser. Mater. Sci. Eng. 18, 102019 (2011) http://dx.doi.org/10.1088/1757-899X/18/10/102019

[16] L.S. Cavalcante, J.C. Sczancoski, J.W.M. Espinosa, V.R. Mastelaro, A. Michalowicz,

P.S. Pizani, F.S. De Vicente, M.S. Li, J.A. Varela, E. Longo, J. Alloys Compd. 471, 253 (2009) http://dx.doi.org/10.1016/j.jallcom.2008.03.080

[17] J.Y. Park, J.H. Lee, G.S.R. Raju, B.K. Moon, J.H. Jeong, B.C. Choi, J.H. Kim, Ceram. Int. 40, 5693 (2014) http://dx.doi.org/10.1016/j.ceramint.2013.11.007

[18] Y. Kaihatsu, W.N. Wang, F. Iskandar, K. Okuyama, Mater. Lett. 64, 836 (2010) http://dx.doi.org/10.1016/j.matlet.2010.01.033

[19] C. Lin, M. Yu, Z. Cheng, C. Zhang, Q. Meng, J. Lin, Inorg. Chem. 47, 49 (2008) http://dx.doi.org/10.1021/ic700652v

[20] T. Hayakawa, A. Hiramitsu, M. Nogami, Appl. Phys. Lett. 82, 2975 (2003) http://dx.doi.org/10.1063/1.1569038

[21] M. Anicete-Santos, F.C. Picon, M.T. Escote, E.R. Leite, P.S. Pizani, J.A. Varela, E. Longo, Appl. Phys. Lett. 88, 211913 (2006) http://dx.doi.org/10.1063/1.2207491

[22] E. Orhan, M. Anicete-Santos, M.A.M.. Maurera, F.M. Pontes, A.G. Souza, J. Andrès, A. Beltràn, J.A. Varela, P.S. Pizani, C.A. Taft, E. Longo, J. Solid State Chem. 178, 1284 (2005) http://dx.doi.org/10.1016/j.jssc.2004.12.038

[23] F. Gu, S.F. Wang, M.K. Lü, G.J. Zhou, D. Xu, D.R. Yuan, J. Phys. Chem. B 108, 8119 (2004) http://dx.doi.org/10.1021/jp036741e

[24] Y. Hu, H.J. Chen, Mater. Res. Bull. 43, 2153 (2008) http://dx.doi.org/10.1016/j.materresbull.2007.09.002

[25] W.N. Wang, T. Ogi, Y. Kaihatsu, F. Iskandar, K. Okuyama, J. Mater. Chem. 21, 5183 (2011) http://dx.doi.org/10.1039/c0jm02215b

[26] X. Zhang, Z. Lu, H. Liu, J. Lin, X. Xu, F. Meng, J. Zhao, C. Tang, J. Mater. Chem. C 3, 3311 (2015) http://dx.doi.org/10.1039/c5tc00179j

[27] T. Ogi, Y. Kaihatsu, F. Iskandar, W.N. Wang, K. Okuyama, Adv. Mater. 20, 3235 (2008) http://dx.doi.org/10.1002/adma.200702551

[28] I. Villa, A. Vedda, M. Fasoli, R. Lorenzi, N. Kränzlin, F. Rechberger, G. Ilari, D. Primc, B. Hattendorf, F.J. Heiligtag, M. Niederberger, A. Lauria, Chem. Mater. 28, 3245 (2016) http://dx.doi.org/10.1021/acs.chemmater.5b03811

[29] V.F. Guimarães, L.J.Q.Q. Maia, I. Gautier-Luneau, C. Bouchard, A.C. Hernandes, F. Thomas, A. Ferrier, B. Viana, A. Ibanez, J. Mater. Chem. C 3, 5795 (2015) http://dx.doi.org/10.1039/C5TC00237K

[30] Ibanez Alain; Ferraz Guimaraes Vinicius; Maia Lauro June Queiroz; Hernandes Antonio Carlos, Luminophore composition for UV-visible light conversion and light converter obtained therefrom, WO/2012/085290 (2012) https://patentscope.wipo.int/search/en/detail.jsf?docId=WO2012085290

[31] V.F. Guimarães, M. Salaün, P. Burner, L.J.Q.Q. Maia, A. Ferrier, B. Viana, I. Gautier-Luneau, A. Ibanez, Solid State Sci. 65, 6 (2017) http://dx.doi.org/10.1016/J.SOLIDSTATESCIENCES.2016.12.011

[32] H. Deters, A.S.S. de Camargo, C.N. Santos, C.R. Ferrari, A.C. Hernandes, A. Ibanez, M.T. Rinke, H. Eckert, J. Phys. Chem. C 113, 16216 (2009) http://dx.doi.org/10.1021/jp9032904

[33] S. Sen, Z. Xu, J.F. Stebbins, J. Non. Cryst. Solids 226, 29 (1998) http://dx.doi.org/10.1016/S0022-3093(97)00491-2

[34] L. Kerns, M.C. Weinberg, S. Myers, R. Assink, J. Non. Cryst. Solids 232–234, 86 (1998) http://dx.doi.org/10.1016/S0022-3093(98)00376-7

[35] G. Dong, X. Liu, X. Xiao, Q. Zhang, G. Lin, Z. Ma, D. Chen, J. Qiu, Electrochem. Solid-State Lett. 12, K53 (2009) http://dx.doi.org/10.1149/1.3137021

[36] V.F. Guimarães, A.D. Sontakke, L.J.Q.Q. Maia, M. Salaün, I. Gautier-Luneau, A. Ferrier, B. Viana, A. Ibanez, J. Lumin. 188, 448 (2017) http://dx.doi.org/10.1016/j.jlumin.2017.05.013

[37] P. Burner, A.D. Sontakke, M. Salaün, M. Bardet, J.-M.M. Mouesca, S. Gambarelli, A.-L.L. Barra, A. Ferrier, B. Viana, A. Ibanez, others, V. Maurel, I. Gautier-Luneau, Angew. Chemie - Int. Ed. 129, 14183 (2017) http://dx.doi.org/10.1002/anie.201706070

[38] P.P. Neves, L.J.Q. Maia, M.I.B. Bernardi, A.R. Zanatta, V.R. Mastelaro, S.M. Zanetti, E.R. Leite, J. Sol-Gel Sci. Technol. 29, 89 (2004) http://dx.doi.org/10.1023/B:JSST.0000023010.79540.6f

[39] J.F. Carvalho, F.S. De Vicente, S. Pairis, P. Odier, A.C. Hernandes, A. Ibanez, J. Eur. Ceram. Soc. 29, 2511 (2009) http://dx.doi.org/10.1016/j.jeurceramsoc.2009.03.005

[40] D. Massiot, F. Fayon, M. Capron, I. King, S. Le Calvé, B. Alonso, J.-O. Durand, B. Bujoli, Z. Gan, G. Hoatson, Magn. Reson. Chem. 40, 70 (2002) http://dx.doi.org/10.1002/mrc.984

[41] G. te Velde, E.J. Baerends, J. Comput. Phys. 99, 84 (1992) http://dx.doi.org/10.1016/0021-9991(92)90277-6

[42] S.H. Vosko, L. Wilk, M. Nusair, Can. J. Phys. 58, 1200 (1980) http://dx.doi.org/10.1139/p80-159

[43] A.D. Becke, Phys. Rev. A 38, 3098 (1988) http://dx.doi.org/10.1103/PhysRevA.38.3098

[44] J.P. Perdew, Phys. Rev. B 33, 8822 (1986) http://dx.doi.org/10.1103/PhysRevB.33.8822

[45] E. van Lenthe, A. Ehlers, E.-J. Baerends, J. Chem. Phys. 110, 8943 (1999) http://dx.doi.org/10.1063/1.478813

[46] D. Mazza, M. Vallino, G. Busca, J. Am. Ceram. Soc. 75, 1929 (1992)

http://dx.doi.org/10.1111/j.1151-2916.1992.tb07219.x

[47] H. You, G. Hong, J. Phys. Chem. Solids 60, 325 (1999) http://dx.doi.org/10.1016/S0022-3697(98)00290-X

[48] M. Okuno, N. Zotov, M. Schmücker, H. Schneider, J. Non. Cryst. Solids 351, 1032 (2005) http://dx.doi.org/10.1016/j.jnoncrysol.2005.01.014

[49] P. Tarte, Spectrochim. Acta Part A Mol. Spectrosc. 23, 2127 (1967) http://dx.doi.org/10.1016/0584-8539(67)80100-4

[50] E.I. Kamitsos, M.A. Karakassides, G.D. Chryssikos, J. Phys. Chem. 91, 1073 (1987) http://dx.doi.org/10.1021/j100289a014

[51] C.N. Santos, D. De Sousa Meneses, P. Echegut, D.R. Neuville, A.C. Hernandes, A. Ibanez, Appl. Phys. Lett. 94, 151901 (2009) http://dx.doi.org/10.1063/1.3115796

[52] S. Rada, M. Culea, M. Rada, P. Pascuta, V. Maties, E. Culea, J. Mol. Struct. 937, 70 (2009) http://dx.doi.org/10.1016/j.molstruc.2009.08.016

[53] L.J.Q.Q. Maia, C.R. Ferrari, V.R. Mastelaro, a. C. Hernandes, A. Ibanez, Solid State Sci. 10, 1835 (2008) http://dx.doi.org/10.1016/j.solidstatesciences.2008.03.031

[54] R.X. Fischer, V. Kahlenberg, D. Voll, K.J.D. MacKenzie, M.E. Smith, B. Schnetger, H.J. Brumsack, H. Schneider, Am. Mineral. 93, 918 (2008) http://dx.doi.org/10.2138/am.2008.2744

[55] E. Mendelovici, R. Villalba, A. Sagarzazu, O. Carias, Clay Miner. 30, 307 (1995) http://dx.doi.org/10.1180/claymin.1995.030.4.04

[56] A.D. Sontakke, M. Salaün, V.F. Guimarães, A. Ferrier, L. Maia, I. Gautier-Luneau, B. Viana, A. Ibanez, Light. Diodes Mater. Devices, Appl. Solid State Light. XXI 10124, 1012409 (2017)